Automated seismic acquisition geometry design for optimized illumination at the target a linearized approach

Wu, Sixue; Verschuur, Dirk J.; Blacquiere, Gerrit

DOI
10.1109/TGRS.2021.3131365

Publication date
2021

Document Version
Final published version

Published in
IEEE Transactions on Geoscience and Remote Sensing

Automated Seismic Acquisition Geometry Design for Optimized Illumination at the Target: A Linearized Approach

Sixue Wu, Dirk J. Verschuur, and Gerrit Blacquière

***Abstract*— In seismic exploration methods, imperfect spatial sampling at the surface causes a lack of illumination at the target in the subsurface. The hampered image quality at the target area of interest causes uncertainties in reservoir monitoring and production, which can have a substantial economic impact. Especially in the case of a complex overburden, the impact of surface sampling on target illumination can be significant. The target-oriented acquisition analysis based on wavefield propagation and a known velocity model has been used to provide guidance for optimizing the acquisition parameters. Seismic acquisition design is usually a manual optimization process, with consideration of many aspects. In this study, we develop a methodology that automatically optimizes an irregular receiver geometry when the source geometry is fixed or vice versa. The methodology includes objective functions defined by two criteria: optimizing the image resolution and optimizing the angle-dependent illumination information. We use a two-step parameterization in order to make the problem more linear and, thereby, solve the acquisition design problem by using a gradient descent algorithm. With simple and complex velocity models, we demonstrate that the proposed method is effective, while the involved computational cost is acceptable. Interestingly, the optimization results in our examples show that the conventional uniform geometry already satisfies the resolution requirement, while optimizing for angle coverage can provide a large uplift and is strongly dependent on the velocity model.**

***Index Terms*— Computational seismology, controlled source seismology, image processing, inverse theory, seismic instruments.**

I. Introduction

SEISMIC exploration is an expensive methodology. To ensure optimum data quality with a limited budget, seismic acquisition needs to be designed carefully. One of the important factors that influence both the data quality and the cost is seismic acquisition geometry. It should be designed such that the acquired data meet the quality requirements.

Manuscript received March 29, 2021; revised July 17, 2021 and October 7, 2021; accepted October 18, 2021. Date of publication November 30, 2021; date of current version February 21, 2022. This work was supported by the Delft University of Technology, The Netherlands. *(Corresponding author: Sixue Wu.)*

Sixue Wu was with the Department of Imaging Physics, Delft University of Technology, 2628 CJ Delft, The Netherlands. She is now with BP p.l.c., Sunbury-on-Thames TW16 7LN, U.K. (e-mail: sixuewu.cug@gmail.com).

Dirk J. Verschuur is with the Department of Imaging Physics, Delft University of Technology, 2628 CJ Delft, The Netherlands.

Gerrit Blacquière is with the Department of Geoscience and Engineering, Delft University of Technology, 2628 CN Delft, The Netherlands.

Digital Object Identifier 10.1109/TGRS.2021.3131365

In classical acquisition design, geometries are decided prior to the acquisition based on the basic geological information, such as target depth and maximum reflector dip angle [1]. This approach ensures that the overall seismic image has good resolution, good angle coverage, and a high signal-to-noise ratio. However, certain targets can be inadequately imaged due to the complex geological overburden [2], [3]. The hampered image quality at the target area of interest can cause high uncertainties in reservoir monitoring and production, which can lead to high expenses. In such a circumstance where the subsurface information is already available, the acquisition geometry can be optimized to ensure the image quality at the target area.

Model-based acquisition analysis is a well-established approach to help us design a better acquisition geometry that ensures improved image quality at the target of interest. It uses modeling methods based on ray-tracing, the one-way wave equation, and the two-way wave equation to compute the illumination criteria to appraise the acquisition geometry. This analysis is feasible because the macrosubsurface velocity model with major reflectors is mostly available before the acquisition, especially in a monitoring scenario. This *a priori* velocity model is used for modeling wavefield attributes that can indicate the illumination quality. For example, Muerdter and Ratcliff [4] use ray-trace modeling; Volker *et al.* [5] and Van Veldhuizen *et al.* [6] use one-way wave equation modeling; Regone [7] and Gardner *et al.* [8] use finite-difference modeling; and Kumar *et al.* [9] use full wavefield modeling that includes multiple scattering wavefields. The results from these model-based acquisition analysis methods qualify the target illumination property of the acquisition geometry and enable us to redesign the acquisition by changing the acquisition parameters to fulfill the illumination requirements. The acquisition geometry is usually optimized by manually changing the acquisition parameters in the analysis until its illumination quality is acceptable.

Automated acquisition design can be realized by using optimization methods. Depending on the types of criteria, the methods can be divided into two categories. One category is using statistical methods to optimize the acquisition parameters. This type of method aims to minimize the error that is projected from the data space to the model space by changing the acquisition geometry [10]–[15]. The other category is a deterministic method, which is based on physical models.

For instance, Araya-Polo *et al.* [16] describe a submodular optimization algorithm, and Latiff *et al.* [17] describe a particle swarm algorithm to optimize the acquisition parameters. Both types of methods face the challenges of large parameter space and the nonlinearity of the design problem. Research has shown that global optimization algorithms are effective for solving nonlinear problems; however, the computational costs remain high [18]. Linearized optimization algorithms are fast. However, linearization between the current sampling parameters and the illumination criteria is nontrivial since the sampling parameters are the spatial coordinates of the sampling points.

We introduce a two-step approach to parameterize the acquisition design problem via the density sampling function such that it can be solved by a linearized optimization algorithm. We focus on stationary geometries so that focal beam analysis can be conveniently used to qualify the illumination property in relation to the acquisition geometry. An optimization problem is formulated based on two illumination criteria (image resolution and illumination angle diversity), and a gradient method is used to solve it. The corresponding computational cost is low compared to global optimization methods. In this work, we consider a known velocity model, stationary geometries, and illumination criteria. The most suitable scenario would be an ocean bottom node (OBN) type of survey or a floating cable type of survey [19] in a reservoir monitoring scenario in the marine environment since the main criterion in the marine seismic acquisition is the illumination coverage, while, in land seismic acquisition, we should also consider aspects, such as the surface-wave noise suppression and the signal-to-noise ratio in the design besides illumination criteria.

In the following of this article, first, we define the illumination criteria as the results of focal beam analysis in Section II. Next, we optimize the spatial sampling for the illumination criteria in Section III. Numerical examples, including analyses with regard to the inversion parameter and the effects of a velocity error, are presented in Section IV. Features and limitations of the method are discussed in Section V. Finally, our conclusions are drawn in Section VI.

II. Illumination Criteria

We use focal beam analysis as the forward model to compute the illumination quality criteria in terms of two focal functions: the resolution function and the amplitude-versus-ray parameter (AVP) function, for stationary geometries. The focal beam analysis is a model-based acquisition analysis method. It can appraise the influence of the acquisition geometry in terms of the image resolution and angle-dependent amplitude information [5], [6], [9], [20]. In this section, we review the key formulations of focal beam analysis with respect to primary reflections of the acoustic wavefield in preparation for solving the inverse problem.

A. Resolution Function

The formulation of focal beam analysis is based on the modeling approximation of the wave equation, where the wavefield is described by downgoing and upgoing wavefield extrapolations [21]. Detailed derivations from the acoustic wave equation to the one-way wavefield extrapolation operators can be found in [22].

The resolution function is defined as the con-focal image of a unit reflection point at the target location $\mathbf{r}_k$ [23]. We can write the following expression for each frequency component:

$$P(\mathbf{r};\mathbf{r}_k)=\int_{A_r}\int_{A_s}F(\mathbf{r},\mathbf{r}_r)D(\mathbf{r}_r)W(\mathbf{r}_r,\mathbf{r}_k)R_k \times W(\mathbf{r}_k,\mathbf{r}_s)S(\mathbf{r}_s)F(\mathbf{r}_s,\mathbf{r})d\mathbf{r}_r d\mathbf{r}_s \quad (1)$$

with

$$D(\mathbf{r}_r)=\sum_{m=1}^{N_r}\delta(\mathbf{r}_r-\mathbf{r}_m) \quad (2)$$

and

$$S(\mathbf{r}_s)=\sum_{l=1}^{N_s}\delta(\mathbf{r}_s-\mathbf{r}_l) \quad (3)$$

where $\mathbf{r}_r=(x_r,y_r,z_r)$ and $\mathbf{r}_s=(x_s,y_s,z_s)$ are the lateral locations of receivers and sources at the acquisition levels, respectively; $\mathbf{r}_k=(x_k,y_k,z_k)$ is the target location in the subsurface at the target depth level z_k; $\mathbf{r}=(x,y,z_k)$ are the lateral locations at the target depth level z_k; A_r and A_s are the areas where the receivers and sources are located, respectively; and $P(\mathbf{r};\mathbf{r}_k)$ represents the monochromatic resolution function of the target at $\mathbf{r}_k$. The forward wavefield propagation operators $W(\mathbf{r}_k,\mathbf{r}_s)=((\partial G(\mathbf{r}_k,\mathbf{r}_s))/\partial z)$ extrapolate the source wavefields to the target and $W(\mathbf{r}_r,\mathbf{r}_k)=((\partial G(\mathbf{r}_r,\mathbf{r}_k))/\partial z)$ extrapolate the reflected wavefield from the target to the receiver locations, where G represents the acoustic Green's function in the frequency domain. They are the so-called Rayleigh-II integrals in acoustical and seismic literature. The focusing operators $F=W^*$ focus on the wavefields recorded at the acquisition levels to the target point. For stationary geometries, the receiver and source sampling functions $D(\mathbf{r}_r)$ and $S(\mathbf{r}_s)$ can be expressed as the sums of delta functions, where $\mathbf{r}_m$ and $\mathbf{r}_l$ are the discrete receiver and source locations at the surface acquisition level z_r and z_s, respectively; and N_r and N_s are the number of receivers and the number of shots, respectively. In the case of nonflat topography, all sources and receivers are redatumed to the acquisition levels z_r and z_s, respectively. Since we assume a unit reflection point, the reflectivity at the target R_k has the value of one. Equation (1) can also be seen as the point spread function for analyzing the acquisition imprint: the term $W(\mathbf{r}_r,\mathbf{r}_k)R_kW(\mathbf{r}_k,\mathbf{r}_s)$ represents seismic prestack reflection data; afterward, it is sampled by $D(\mathbf{r}_r)$ and $S(\mathbf{r}_s)$, and refocused via the operators $F(\mathbf{r},\mathbf{r}_r)$, $F(\mathbf{r}_s,\mathbf{r})$ to the target depth level.

Using the definition of focal beams, the above equation can be expressed as

$$P(\mathbf{r};\mathbf{r}_k)=B_r(\mathbf{r};\mathbf{r}_k)B_s(\mathbf{r};\mathbf{r}_k) \quad (4)$$

with

$$B_r(\mathbf{r};\mathbf{r}_k)=\int_{A_r}F(\mathbf{r},\mathbf{r}_r)D(\mathbf{r}_r)W(\mathbf{r}_r,\mathbf{r}_k)d\mathbf{r}_r \quad (5)$$

and

$$B_s(\mathbf{r};\mathbf{r}_k) = \int_{A_s} W(\mathbf{r}_k,\mathbf{r}_s)S(\mathbf{r}_s)F(\mathbf{r}_s,\mathbf{r})d\mathbf{r}_s \tag{6}$$

where B_r and B_s are the focal receiver and source beams, respectively. Equation (4) indicates that the resolution function can be obtained by a multiplication of the source and receiver beams in the space–frequency domain. The definitions of focal beams in (5) and (6) represent the backpropagation of the emitted source wavefield and the recorded receiver wavefield. The source beam B_s shows how well the target can be illuminated from the source side, and the receiver beam B_r shows how well the reflected wavefield can be recorded from the receiver side. Note that the decoupling of the receiver and the source beam can only be applied for stationary source and receiver geometries; in other words, the receiver locations are the same for every source location and vice versa. The receivers and sources do not have to be on the same depth level; they can be redatumed to the same depth level in our wavefield modeling approach. With the known propagation and focusing operator, we can quantitatively evaluate the acquisition influence from the receiver and source geometries by the focal beams. The resolution function indicates the illumination quality by the combined imprint of the source and receiver geometries in the spatial domain. Two attributes of the resolution function are the peak amplitude and the width of the main peak. Sidelobes are related to spatial aliasing. The formulation here is for a single frequency component. The broadband resolution function is obtained by summing over all monochromatic resolution functions, that is to say, applying an imaging condition.

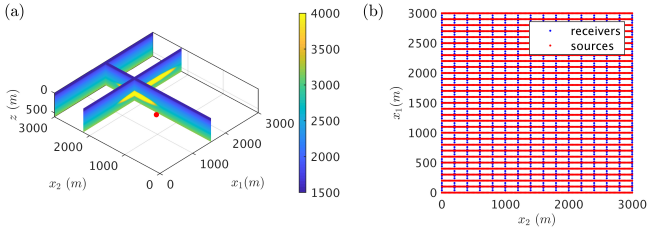

Fig. 1. (a) 3-D velocity model with a target point located at (1500 m, 1500 m, 525 m). (b) Example acquisition geometry, where the blue dots represent the receivers and the red dots represent the sources. The receiver point interval is 40 m, and the line interval is 200 m; the source point interval is 20 m, and the line interval is 100 m.

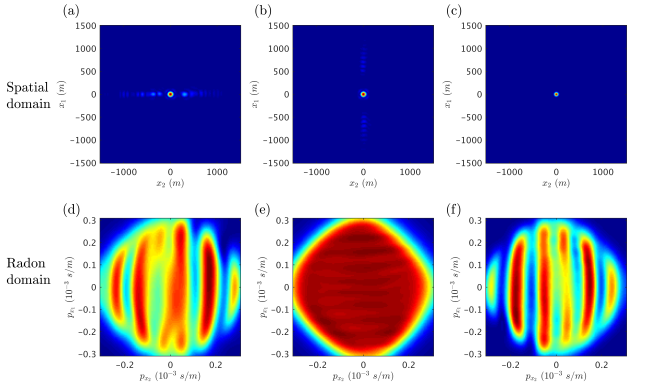

Fig. 2. Broadband focal beam analysis result of the example geometry: (a) focal receiver beam in the spatial domain, (b) focal source beam in the spatial domain, (c) resolution function, (d) focal receiver beam in the linear radon domain, (e) focal source beam in the linear radon domain, and (f) AVP function.

B. AVP Function

The AVP function is defined as the bifocal image of an angle-independent, unit reflector at target depth in the linear radon domain. We can write the bifocal image in the space–frequency domain as follows:

$$P(\mathbf{r}_j;\mathbf{r}_k) = \int_{A_r}\int_{A_s}\int_{A_k}\int_{A_k} F(\mathbf{r}_j,\mathbf{r}_r)D(\mathbf{r}_r)W(\mathbf{r}_r,\mathbf{r}')R(\mathbf{r}'-\mathbf{r}) \times W(\mathbf{r},\mathbf{r}_s)S(\mathbf{r}_s)F(\mathbf{r}_s,\mathbf{r}_k)d\mathbf{r}'d\mathbf{r}d\mathbf{r}_r d\mathbf{r}_s \tag{7}$$

where $\mathbf{r}_j = (x_j, y_j, z_k)$ varies laterally around the target point at $\mathbf{r}_k$, $\mathbf{r}' = (x', y', z_k)$ denotes a lateral location on the target depth level z_k, and A_k is an area at the target depth level. The reflectivity $R(\mathbf{r}'-\mathbf{r}) = \delta(\mathbf{r}'-\mathbf{r})$ is a delta function, representing an angle-independent reflection [24], since the goal is to estimate the geometry imprint instead of the angle-dependent reflectivity. Assuming stationary geometries and local homogeneity around $\mathbf{r}_k$, (7) can be written as a spatial convolution of the receiver beam and the complex conjugate of the source beam [23]. Therefore, the AVP function can be simplified as a multiplication of the receiver beam after reversing the ray parameters and the source beam in the linear radon domain

$$P(\mathbf{p};\mathbf{r}_k) = B_r(-\mathbf{p};\mathbf{r}_k)B_s(\mathbf{p};\mathbf{r}_k) \tag{8}$$

where $\mathbf{p}$ is the ray parameter vectors and $P(\mathbf{p};\mathbf{r}_k)$ represents the monochromatic AVP function of the target at $\mathbf{r}_k$. The focal receiver and source beams in the linear radon domain, $B_r(\mathbf{p};\mathbf{r}_k)$ and $B_s(\mathbf{p};\mathbf{r}_k)$, show the angles of detection from the target and the angles of illumination from the target, respectively. The AVP function shows the angle-dependent illumination quality influenced by the combined receiver and source geometries. The attributes of the AVP function are spatial bandwidth and spectral completeness. The broadband AVP function is obtained by summing the monochromatic AVP functions along lines of constant ray parameter [25].

C. Example of Focal Beam Analysis

We use a simple 3-D velocity model to illustrate the illumination criteria defined by the focal beam analysis. The frequency range is chosen as 5–40 Hz. The velocity model with a salt body is displayed in Fig. 1(a), and a target point is located at $(x_1, x_2, z) = (1500\text{ m}, 1500\text{ m}, 525\text{ m})$. For the chosen target point, the receiver and source geometries shown in Fig. 1(b) are assessed, and the broadband focal beam analysis results are shown in Fig. 2. The focal receiver and source beams can show the focusing and detecting abilities of the receiver and source geometries separately in the spatial domain [see Fig. 2(a) and (b)] and the azimuth angle coverage in the linear radon domain [see Fig. 2(d) and (e)]. In this example, the maximum propagation angle is set to 50°; thus, the angle of illumination is limited. The resolution function in

Fig. 2(c) is the multiplication of the focal beams in the spatial domain. The AVP function in Fig. 2(f) is the multiplication of the focal receiver beam in Fig. 2(d) after reversing the ray parameters and the focal source beam in Fig. 2(e) in the linear radon domain.

Fig. 1(b) shows an example acquisition geometry, where the receiver point interval is 40 m, and the line interval is 200 m; the source point interval is 20 m, and the line interval is 100 m. Due to large receiver and source line intervals, the focal receiver beam has sidelobes in the x_2-direction, and the focal source beam has sidelobes in the x_1-direction in the spatial domain. By virtue of the orthogonal aliasing directions in the receiver and source cross-lines, the aliasing effects cancel out in the resolution function, which shows a desired spiky peak in Fig. 2(c). Fig. 2(d) shows missing angles because the receivers are sparsely sampled in the x_2-direction. The focal source beam in Fig. 2(e) shows a full angle coverage, and no missing angles because the source sampling in the x_1-direction is sufficient. However, the resulting AVP function has even more missing angles since it shows the combined influence from both source and receiver geometries. Note that the resolution and AVP functions are two interconnected aspects of the same illumination property. Resolution concerns the angle-averaged image accuracy, and the AVP function describes the angle-dependent information. The averaged reflectivity over all azimuth angles in Fig. 2(f) gives a good structural image of the given target point in Fig. 2(c). However, the receiver geometry needs to be improved if a full-azimuth angle coverage is desired at the target point (e.g., for an azimuth-dependent AVO analysis). In this section, we have shown the focal receiver and source beams to explain the computation of the focal functions. For the inverse problem in the following, we will only use the focal functions as the illumination criteria.

III. Acquisition Design as an Optimization Process

Automated acquisition design is the inverse problem of acquisition analysis, where the unknown is the sampling geometry. We solve the inverse problem as an optimization problem, where we aim to update the acquisition geometry for optimum target illumination. In the forward model of focal beam analysis, there are seven aspects that can influence the focal beam result, that is to say, the target location, the velocity model, the frequency range, the wavefield modeling and migration operators, and the source and receiver samplings on the acquisition surface. As described in the introduction, the velocity model is known as *a priori* knowledge. To reduce the inversion parameters, we allow the parameters—the target, the frequency range, the wavefield modeling, and migration operators—to be user-defined in advance. A flowchart of the optimization method is shown in Fig. 3, where the steps in the green boxes are the input, and the step in the yellow box is updating the acquisition geometry. The focal functions are computed for each updated geometry and compared to the requirement. Ideally, the updating process stops when the focal functions reach the requirement. The challenges of solving this optimization problem are a large amount of parameters, nonlinearity, and high computational cost. We will address these aspects in the following.

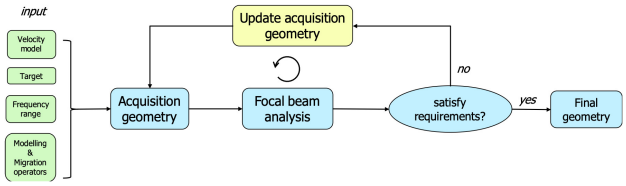

Fig. 3. Workflow of optimizing the receiver geometry for target illumination with a fixed source geometry.

Fig. 4. Feature of the sampling density transformation: (a) horizontal gradient map is transformed to and (b) a set of sampling points whose spatial density distribution is proportional to the input gradient map.

A. Parameterization

We use a strategy that contains two steps to parameterize the acquisition design problem. First, the sampling density, which is defined as the number of sampling points per unit area, is chosen as the continuous parameter of the inverse problem. Second, we transform the density distribution into a realization of a sampling geometry via the weighted centroidal Voronoi diagram [26]. In a 2-D space, the Voronoi diagram partitions the plane into regions based on the weight given by the continuous density function; the centroids of Voronoi cells are then the sampling locations; and this process can be done by Lloyd's algorithm [27]. Thus, this transformation distributes the centroids with a spatial distance that is inversely proportional to the local density value. We can express the discrete receiver locations $\{\mathbf{r}_m\}$ and the discrete source locations $\{\mathbf{r}_l\}$ as follows:

$$\{\mathbf{r}_m\} = f(\phi(\mathbf{r}_r)) \tag{9}$$

and

$$\{\mathbf{r}_l\} = f(\phi(\mathbf{r}_s)) \tag{10}$$

where $\phi(\mathbf{r}_r)$ and $\phi(\mathbf{r}_s)$ represent the sampling receiver and source densities at each lateral location $\mathbf{r}_r$ and $\mathbf{r}_s$, respectively; $f(\cdot)$ denotes the process from a density distribution to a discrete set of points representing the sampling geometry; $\phi(\mathbf{r}_r)$ is normalized such that the sum of $\phi(\mathbf{r}_r)$ is N_r, the total number of receivers; and $\phi(\mathbf{r}_s)$ is normalized such that the sum of $\phi(\mathbf{r}_s)$ is N_s, the total number of sources. Fig. 4(a) shows a general example of the sampling density, where dark colors represent high values and light colors represent low values. Fig. 4(b) shows the sampling map after applying the weighted centroidal Voronoi diagram algorithm. With a predefined total number of samples, the resulting sampling is dense where the density value is high, and the sampling is sparse where the density value is low.

The transformation function has a nondeterministic characteristic: it can generate completely different sampling sets from the same input density distribution because the transformation algorithm uses a random number generator. On the one hand,

this characteristic allows the actual sampling locations to be flexible. The parameter—sampling density—can be seen as a macrosolution of the acquisition geometry, which can be used for flexible acquisition systems, regular acquisition systems, and potentially automated devices. On the other hand, this characteristic causes uncertainty in the illumination quality, which is assessed by the focal functions that depend on the realization of the sampling geometry. This aspect will be analyzed in numerical examples. Overall, we are able to linearize the relationship between the parameters and the illumination criteria, by using the continuous density function instead of the spatial coordinates of all individual sampling points as parameters, and by turning the density-to-sampling transformation into a separate step.

B. Consider the Receiver Side

To further reduce the inversion parameters, we consider optimizing only the receiver geometry when the source geometry is fixed or vice versa. The scenario of a fixed source geometry is used to formulate the inversion method. The methodology holds likewise for optimizing the source geometry with a fixed receiver geometry because sources and receivers are interchangeable due to reciprocity [28]. The resolution and the angle distribution at the target can be represented by the resolution function and the AVP function, respectively. The reference resolution and AVP function can be user-defined (e.g., a perfect spike resolution function and a flat AVP function). In this article, we choose the resolution and AVP function determined from the full 3-D regular source and receiver geometries, which obeys the Nyquist sampling criterion to be the reference for comparison. The reference geometry is considered to have the best attainable illumination.

This scenario can be considered as determining an optimum OBN layout in the marine environment subject to a limited amount of OBN's and assuming a full 3-D sampling on the source side. The objective of the simplified problem is to automatically optimize a receiver geometry for good illumination of the chosen target, as close to the reference focal functions as possible.

C. Fixed Number of Receivers

A dense spatial sampling that satisfies the Nyquist criterion [29] gives the best illumination achievable. Note that the Nyquist requirement is defined by a regular geometry. Beyond the Nyquist requirement, more spatial sampling can increase fold and, therefore, improves signal-to-noise ratio and, thus, image quality. Below the Nyquist requirement, we expect the illumination improves with increasing receivers until the spatial sampling satisfies the Nyquist criterion [29], on the condition that the geometry of each sampling number is optimum. If we allow the number of sampling points to vary during optimization, an inversion scheme will update the geometry to one of which sampling number is close to the Nyquist requirement. The choice of using an indefinite number of receivers will be discussed in Section V.

In an ideal scenario, the geometry is a full 3-D sampling. However, in practice, the acquisition geometry is limited by economic factors and the number of inventories, such as in a marine seismic acquisition. For the examples in this article, we fix the number of sampling points far below the Nyquist requirement to gain insight into how we can subsample the data below the Nyquist requirement. This represents the scenario of a fixed budget, so we can demonstrate different realizations of sparse irregular geometries obtained by an optimization algorithm. The setting of a fixed number of receivers also reduces the nonlinearity of the problem. However, the optimization problem becomes mathematically not well defined—there is always an error term remaining, and there will exist many geometry solutions of a similar error value. In other words, there is no unique solution. Typically, the amount of stationary equipment is also restricted in practice. In summary, we are dealing with a nonlinear problem with many possible solutions that have the same error.

D. Geometry Optimization for Target Illumination

The resolution function and the AVP function are used as the illumination criteria. They represent two interconnected aspects of the illumination property. They are used to formulate two individual objective functions detailing the purposes of optimizing the image resolution and optimizing the angle-dependent information.

1) Optimizing the Image Resolution: To optimize the image resolution, we have the following objective function:

$$J_1 = \sum_{x,y} ||P(\mathbf{r}, \phi_{\text{ref}}; \mathbf{r}_k) - P(\mathbf{r}, \phi; \mathbf{r}_k)||^2 \tag{11}$$

where $P(\mathbf{r}, \phi_{\text{ref}}; \mathbf{r}_k)$ represents the resolution function from the reference receiver density distribution ϕ_{ref}, which is chosen as a full 3-D sampling that satisfies the Nyquist criterion; $P(\mathbf{r}, \phi; \mathbf{r}_k)$ represents the resolution function from the receiver density to be optimized, ϕ. Thus, it follows that only the image amplitude at target level z_k is considered when comparing to the reference. The gradient is given by substituting (4) and (5) in (11), and taking the derivative of the residual $E(\mathbf{r}; \mathbf{r}_k) = P(\mathbf{r}, \phi_{\text{ref}}; \mathbf{r}_k) - P(\mathbf{r}, \phi; \mathbf{r}_k)$ with respect to ϕ by applying the adjoint method [30]. Note that (11) is formulated for one frequency; the gradient is formulated for a range of frequencies, i.e., a sum over all frequencies. The gradient required is

$$\nabla_\phi J_1 = -2 \sum_{\omega} \int_{A_k} W(\mathbf{r}_r, \mathbf{r}_k) E(\mathbf{r}; \mathbf{r}_k) B_s(\mathbf{r}; \mathbf{r}_k) W^*(\mathbf{r}_r, \mathbf{r}_k) d\mathbf{r} \tag{12}$$

where A_k is an area at the target depth level. From a physics perspective, the multiplication of the source beam B_s and the residual E can be viewed as propagating the residual to the surface, sampled by the source geometry, and backpropagated to the target. After that, the product $E(\mathbf{r}; \mathbf{r}_k) B_s(\mathbf{r}; \mathbf{r}_k)$—the residual now including the source sampling effect—is again forward propagated from the target level to the acquisition surface and then correlated with the upgoing one-way wavefield from the target. In the end, summing over all frequencies can be viewed as applying the imaging condition. Note that

the objective function and the gradient are for one target point. In the case of multiple target points, the objective function and the gradient are summed over all target points.

2) Optimizing the Angle-Dependent Information: To optimize the angle-dependent information, we have the following objective function:

$$J_2 = \sum_{p_x, p_y} ||P(\mathbf{p}, \phi_{\text{ref}}; \mathbf{r}_k) - P(\mathbf{p}, \phi; \mathbf{r}_k)||^2 \tag{13}$$

where $P(\mathbf{p}, \phi_{\text{ref}}; \mathbf{r}_k)$ represents the AVP function from the reference receiver density ϕ_{ref}, and $P(\mathbf{p}, \phi; \mathbf{r}_k)$ represents the AVP function from the variable density ϕ. This criterion means that we consider the angle-dependent imprint that is associated with the target depth level compared to the reference. The reference beam from the full 3-D sampling is considered to have the best attainable angle distribution. Similar to (12), the gradient is given by substituting (8) in (13) and taking the derivative of the residual $E(\mathbf{p}; \mathbf{r}_k) = P(\mathbf{p}, \phi_{\text{ref}}; \mathbf{r}_k) - P(\mathbf{p}, \phi; \mathbf{r}_k)$ with respect to ϕ. The gradient required is

$$\nabla_\phi J_2 = -2 \sum_{\omega} \int_{A_m} W(\mathbf{r}_r, \mathbf{r}_k) \mathcal{L}^{-1}\{E(\mathbf{r}; \mathbf{r}_k) B_s(\mathbf{r}; \mathbf{r}_k)\} \times W^*(\mathbf{r}_r, \mathbf{r}_k) d\mathbf{r} \tag{14}$$

where $\mathcal{L}^{-1}\{\cdot\}$ represents the inverse linear radon transform. From a physics perspective, the gradient estimation can be viewed as combining the residual in the linear radon domain with the source beam in the linear radon domain, transforming to the spatial domain, forward propagating from the target to the acquisition surface, correlating with the one-way wavefield from the target, and applying the imaging condition. Again, the objective function and the gradient are for one target point. In the case of multiple target points, the objective function and the gradient are summed over all target points.

3) Algorithm: We use a gradient descent scheme with a line search procedure to solve the optimization problem. Since the problem is nonlinear and not well defined, different initial guesses are used to find the approachable minimum. Initial guesses are chosen as the one-way wavefield amplitude at the acquisition surface and concentrated circles of different radius above the target. The pseudoalgorithm of geometry optimization using J_1 is given in Algorithm 1. Due to the parameterization approach, the same density distribution can be transformed to different sampling sets that have a range of misfit values and varying gradients. We apply Gaussian smoothing to the calculated gradient to reduce the dependence of one specific sampling set. In addition, we use a predefined maximum number of iterations and select the smallest $J_1(\phi^i)$ after the process is finished. At a later stage of the iteration, there is only a small sampling density update, and density can be seen as nearly repeated. Inherently, the density is transformed to different geometries that may have different J_1 values; therefore, the algorithm accounts for the nondeterministic feature in the parameterization approach. The algorithm of geometry optimization using J_2 follows the same procedure with the corresponding equations replaced in Algorithm 1.

Algorithm 1 Geometry Optimization Using J_1

Input: target location, initial guesses $\phi^0_{1,2,\ldots,N}$, i_{max} (N is the number of initial guesses)

1: **for** each initial guess **do**
2: Set iteration number $i = 1$
3: **while** $i \leq i_{max}$ **do**
4: Transform ϕ to geometry $D(\mathbf{r}_r)$ using the algorithm described in [26]
5: Compute resolution function $P(\mathbf{r}; \mathbf{r}_k)$ by equation 1
6: Compute objective function J_1 by equation 11
7: Compute gradient $\nabla_\phi J_1$ by equation 12, and apply a Gaussian smoothing
8: Line search procedure, select step size α
9: Update density $\phi^{i+1} = \phi^i + \alpha \nabla_\phi J_1$
10: $i = i + 1$
11: **end while**
12: **end for**
13: Select density with the lowest J_1 value

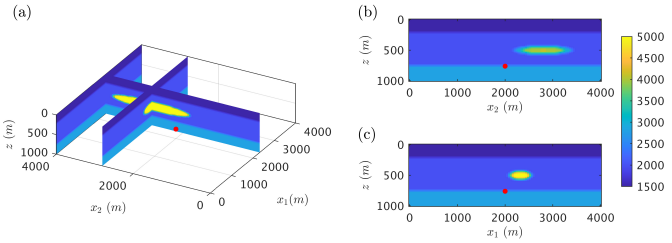

Fig. 5. (a) 3-D velocity model with the target point represented by a red dot and (b) and (c) velocity model cross sections. The spatial coordinate of the target point is (2000 m, 2000 m, 570 m).

IV. Numerical Examples

A. Simple 3-D Salt Model

A simple 3-D velocity model with an ellipsoidal salt body is used to test the method (see Fig. 5). The target point located at a depth of 570 m is indicated by a red dot in the 3-D velocity model. For computational efficiency, the frequency range used here is 5–10 Hz. Based on the Nyquist criterion for a regular geometry, the full 3-D geometry that ensures a minimal aliasing effect for the corresponding bandwidth requires roughly 1400 receivers. This number is estimated by first calculating the Nyquist sampling interval $(c/(2 * f_{\max}))$ using the water velocity $c = 1500$ m/s and then counting the number of receivers on the acquisition surface, where there is wavefield energy modeled by propagating an impulsive response from the target to the acquisition surface. In this example, the source geometry and the reference receiver geometry are full 3-D geometries that satisfy the Nyquist criterion. For geometry optimization, the receiver number is limited to 100, which is around 7% of the Nyquist requirement. Fig. 6 shows that the reference resolution function has no sidelobes, and the AVP function has a full angle coverage. The AVP function has a nonflat spectrum due to the influence of the salt overburden. We consider that the focal functions from the full 3-D sampling on both the source and receiver sides represent the best attainable illumination. We optimize the receiver

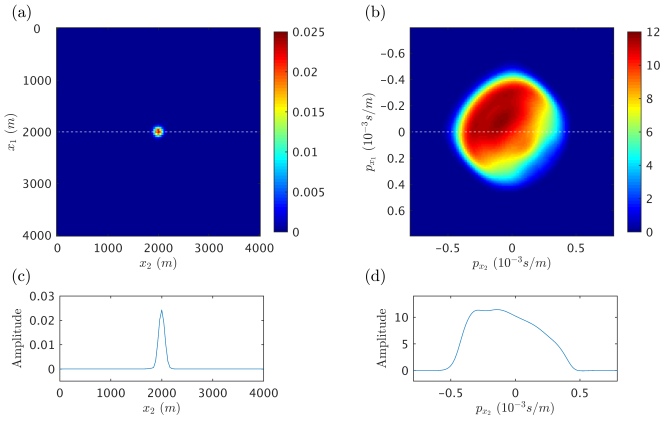

Fig. 6. (a) Reference resolution function, (b) reference AVP function, (c) cross section of (a) at $x_1 = 2000$ m, and (d) a cross section of (b) at $p_{x_1} = 0$ s/m.

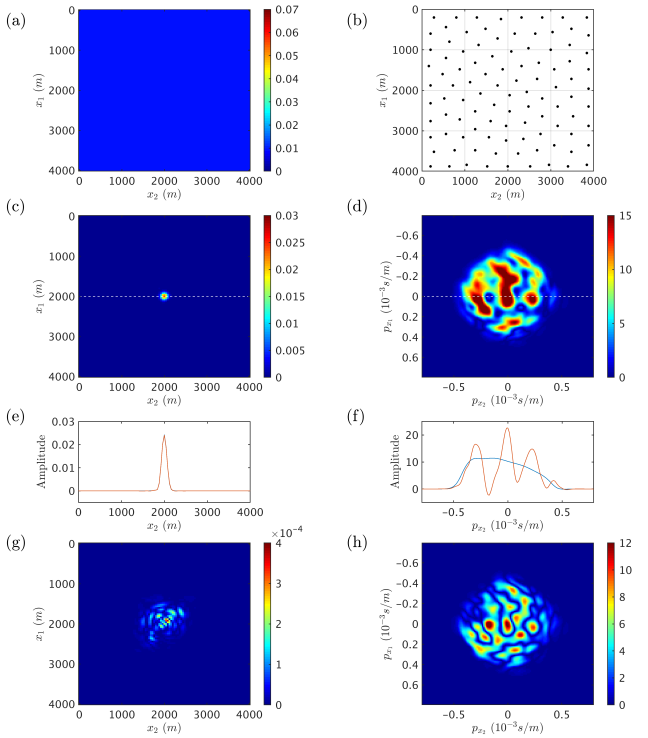

Fig. 7. Focal beam analysis results of a uniform receiver geometry under the simple salt model: (a) receiver density distribution, (b) receiver geometry, (c) corresponding resolution function, and (d) AVP function. The dashed line in (c) and (d) indicates the cross section locations of plots (e) and (f). The red line in (e) and (f) represents the evaluated geometry, while the blue line represents the reference geometry. (g) and (h) Residuals of the resolution function and the AVP function, respectively, displayed in absolute scale.

geometry for a maximum match to the target illumination obtained by the reference receiver geometry by using J_1 and J_2 separately.

Fig. 7 shows the focal beam analysis results of a uniform geometry with 100 receivers. This represents the conventional scenario since OBNs are typically evenly deployed. Fig. 7(a) shows that the acquisition area has a uniform spatial sampling density, which is transformed to the corresponding receiver geometry via the weighted Voronoi algorithm in Fig. 7(b).

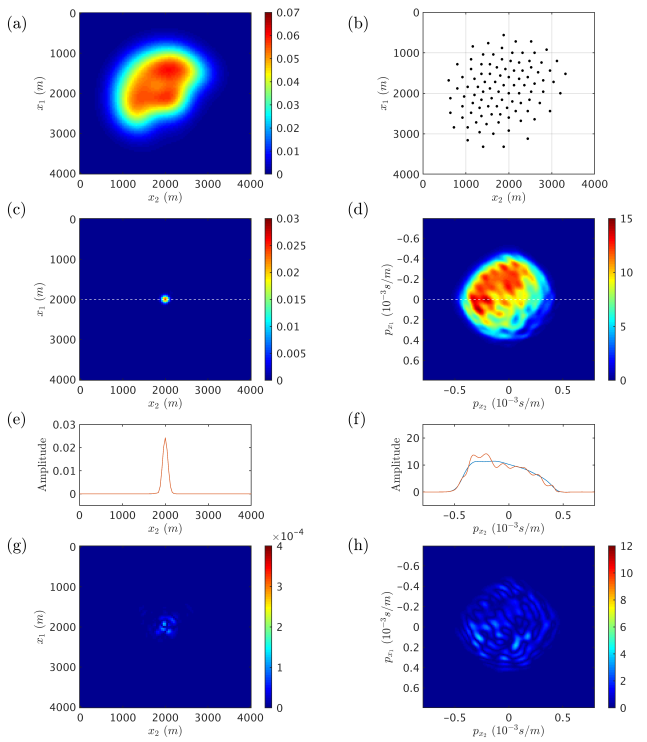

Fig. 8. Geometry optimization results using J_1 under the simple salt model: (a) optimized receiver density distribution, (b) optimized receiver geometry, (c) corresponding resolution function, and (d) AVP function. The dashed line in (c) and (d) indicates the cross section locations of plots (e) and (f). The red line in (e) and (f) represents the evaluated geometry, while the blue line represents the reference geometry. (g) and (h) Residuals of the resolution function and the AVP function, respectively, displayed in absolute scale.

The consequent resolution function has a sharp peak in Fig. 7(c) and 7(e); the residual in Fig. 7(g) is small with the maximum error being 1% of the scale of the resolution function. The resulting AVP function covers high angles with many azimuths in the middle range missing [see Fig. 7(d) and (f)].

Fig. 8 shows the optimization results using J_1, i.e., using the resolution function as the criterion. Compared to the focal analysis results of the uniform geometry, both the residuals of the resolution function and the AVP function have a lower amplitude [see Fig. 8(g) and (h)] although the optimization scheme only uses the resolution function to compute the update. This is probably because the resolution and AVP functions are two interconnected aspects of the same illumination property. Resolution concerns the angle-averaged image accuracy, and the AVP function describes the angle-dependent information. Optimizing for one could lead to certain improvements in the other criterion. Fig. 9 shows the optimization results using J_2, where the AVP function is used as the criterion. It is clearly visible that the residual of the AVP function in Fig. 9(h) is the lowest compared to the residuals in Figs. 7(h) and 8(h), and the cross section of the AVP function in Fig. 9(f) shows the closest match to the reference.

Since the same sampling density distribution can be transformed to different geometry realizations of varying illumination quality, we transform the density distributions in Figs. 7(a), 8(a), and 9(a) each to 100 different geometry

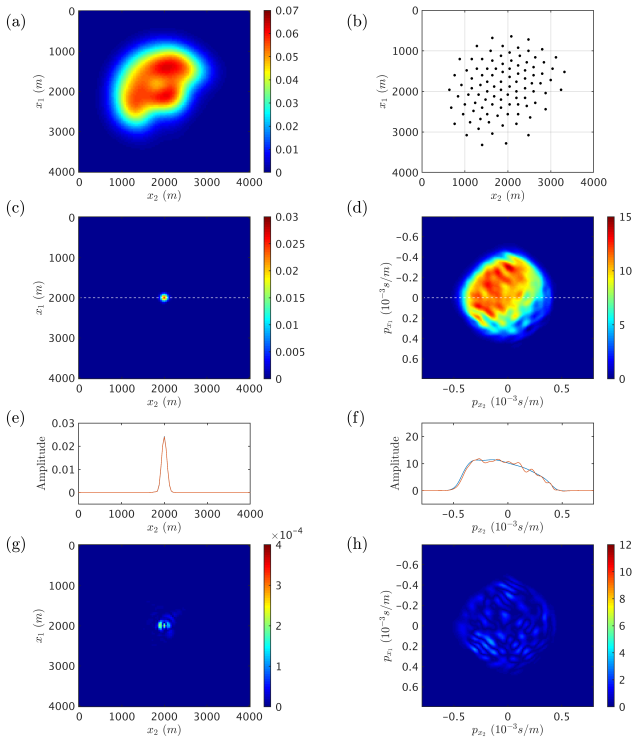

Fig. 9. Geometry optimization results using J_2 under the simple salt model: (a) optimized receiver density distribution, (b) optimized receiver geometry, (c) corresponding resolution function, and (d) AVP function. The dashed line in (c) and (d) indicates the cross section locations of plots (e) and (f). The red line in (e) and (f) represents the evaluated geometry, while the blue line represents the reference geometry. (g) and (h) Residuals of the resolution function and the AVP function, respectively, displayed in absolute scale.

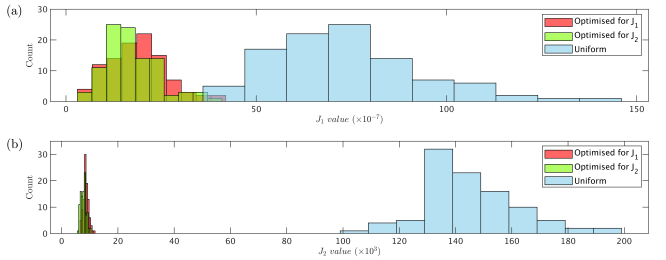

Fig. 10. (a) Histograms of J_1 values of 100 realizations of the receiver density optimized for J_1 (red), the density optimized for J_2 (green), and the uniform density (blue). (b) Histograms of J_2 values of 100 realizations of the density optimized for J_1 (red), the density optimized for J_2 (green), and the uniform density (blue).

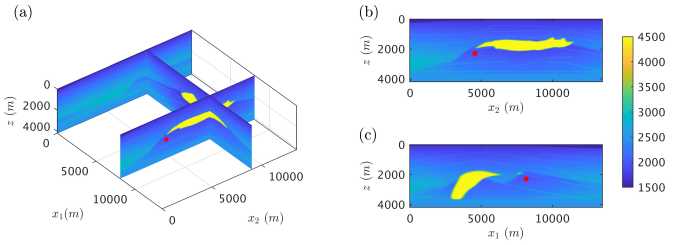

Fig. 11. (a) 3-D SEG /EAGE salt model with the target point represented by a red dot and (b) and (c) velocity model slices where the target is denoted by a red star. The coordinate of the target point is (8160 m, 4560 m, 2300 m).

realizations and analyze their variations in J_1 and J_2 values. Fig. 10(a) presents the histograms of J_1 values calculated from the 100 geometries that are transformed from the density optimized for J_1 (red), the density optimized for J_2 (green), and the uniform density (blue). The density optimized for J_1 shows an improvement in resolution in general: the red histogram has a lower mean value than the blue histogram; and the variation of the red histogram is approximately one-third of the variation of the blue histogram though there is a small overlap between the two histograms. Even though it appears that all density maps have relative large variation in J_1 values, the resolution of three density distributions are all close to the reference—there is no visible error in Figs. 7(e), 8(e), and 9(e).

Fig. 10(b) presents the histograms of J_2 values calculated from the 100 geometries that are transformed from the density optimized for J_1 (red), the density optimized for J_2 (green), and the uniform density (blue). The density optimized for J_2 shows the best angle coverage among the three densities: the mean value of the green histogram is the lowest and much smaller than the blue histogram; the variation of the green histogram is only 10% of the variation of the blue histogram. Compared to Fig. 10(a), there is a larger difference when optimizing for J_2. This makes sense because the resolution is mainly affected by the spatial sampling rate. Since the total amount of sampling points remains the same during optimization, there is not a large improvement in resolution. Furthermore, the histogram distributions of density optimized for J_1 and J_2 overlap each other. This is probably because the density maps optimized for J_1 and J_2 in Fig. 8(a) and 9(a) have high resemblances. From this analysis, we conclude that the variation in objective function values due to the specific geometry realization from the same density function will have an impact on the optimization process, but the effect is acceptable.

The density maps and geometries after optimization are no longer uniform. The spatial variation in the density map indicates the areas that should have a higher sampling rate and the areas that could have a lower sampling rate. There exist other geometry solutions with similar objective function values since the optimization problem is nonlinear and not well-defined. The solution space can be reduced by adding extra constraints, such as acquisition deployment preferences. For instance, there might be areas that are restrictive for stationary receivers. The results show that a uniform geometry already satisfies the resolution requirement; the optimization for J_1 improves the resolution on a small scale; and a larger improvement is limited by the total amount of sampling points. Optimizing for J_2 shows a significant improvement in the angle distribution compared to the uniform geometry. The optimized geometries have a better angle coverage on all azimuths, and the spectrum has small fluctuations compared to the reference.

B. SEG/EAGE Salt Model

The geometry optimization scheme is also tested for a subsampled Society of Exploration Geophysicists (SEG)/European Association of Geoscientists and Engineers (EAGE) salt model [31]. The velocity model is shown

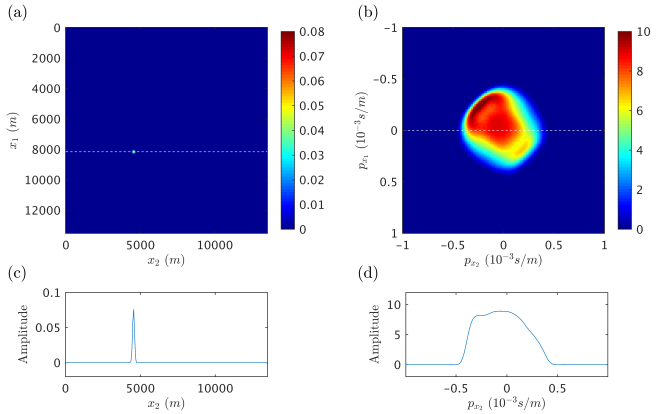

Fig. 12. (a) Reference resolution function, (b) reference AVP function, (c) cross section of (a) at $x_1 = 8000$ m, and (d) cross section of (b) at $p_{x_1} = 0$ s/m.

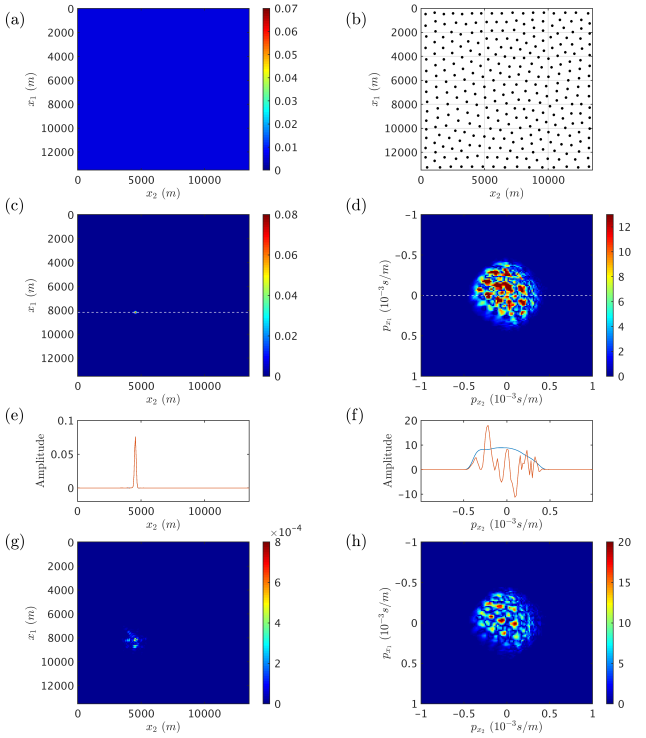

Fig. 13. Focal beam analysis of a uniform receiver geometry under the SEG/EAGE salt model: (a) receiver density distribution, (b) receiver geometry, (c) corresponding resolution function, and (d) AVP function. The dashed line in (c) and (d) indicates the cross section locations of plots (e) and (f). The red line in (e) and (f) represents the evaluated geometry, while the blue line represents the reference geometry. (g) and (h) Residuals of the resolution function and the AVP function, respectively, displayed in absolute scale.

in Fig. 11, and the reference focal functions are shown in Fig. 12. The peak of the resolution function is located at the lateral location of the target. The complex salt overburden has a clear imprint on the AVP function. In this example, the frequency range is 5–10 Hz, and a regular Nyquist sampling requires roughly 7300 receivers. This number is estimated by first calculating the Nyquist sampling interval $(c/(2 * f_{\max}))$ using the water velocity $c = 1500$ m/s and then counting the number of receivers on the acquisition surface, where there is wavefield energy modeled by propagating an impulsive response from the target to the acquisition surface. The source geometry and the reference receiver geometries are full 3-D geometries that satisfy the Nyquist criterion. The receiver number is limited to 300, which is around 4% of the Nyquist requirement.

First, we show the focal beam analysis results of a uniform geometry of 300 receivers (see Fig. 13). The resolution function has a sharp peak in Fig. 13(c) and (e); the misfit in Fig. 13(g) is small with the maximum being 0.8% of the scale of the resolution function. However, there are high-amplitude fluctuations in the AVP function compared to the reference [see Fig. 13(d) and (f)]. Fig. 14 shows the optimization results using J_1, and Fig. 15 shows the optimization results using J_2 with the SEG/EAGE salt model shown in Fig. 11. Comparing the focal functions of these three cases, Fig. 14(g) shows the smallest residual of the resolution function; Fig. 15(h) shows the smallest residual of the AVP function; and the uniform geometry has an acceptable resolution but a high residual in angle coverage.

Because of the uncertainty in illumination quality, again, we transform the densities in Figs. 13(a), 14(a), and 15(a) each to 100 geometries and analyze their variations in J_1 and J_2. Fig. 16(a) presents the histograms of J_1 values calculated from the 100 geometries that are transformed from the density optimized for J_1 (red), the density optimized for J_2 (green), and the uniform density (blue). The density optimized for J_1 shows a small-scale improvement in resolution: the mean value of the red histogram is the lowest though a large portion of it overlaps with the histogram of the uniform density. Note that it may appear that all density maps have relatively large variation in J_1 values; however, they all have an acceptable resolution since the error is barely visible compared to the reference in Figs. 13(e), 14(e), and 15(e).

Fig. 16(b) presents the histograms of J_2 values calculated from the 100 geometries that are transformed from the density optimized for J_1 (red), the density optimized for J_2 (green), and the uniform density (blue). In addition, we repeat the complete optimization process for J_2 ten times to test the overall stability with the inherent uncertainty of the sampling set. The J_2 values of the outcome are plotted as a one-bin histogram (orange) in Fig. 16(b). The density optimized for J_2 has the best angle coverage: the green histogram has the lowest mean value, and its variation is 10% of the variation of the blue histogram. The J_2 values of the ten repeated tests lie within the range of the green histogram. It shows that optimizing for J_2 is stable, despite the variations in geometry realizations during the optimization process.

The density maps and geometries after optimization in Fig. 14(a) have a relatively symmetric shape, while the density map in Fig. 15(a) has an irregular shape. This implies that the resolution requirement is less affected by the complex overburden than the AVP requirement, where the complex overburden can have an asymmetric effect on the geometry. Moreover, optimizing for J_1 already leads to a huge improvement in the AVP function compared to the uniform situation. Nevertheless,

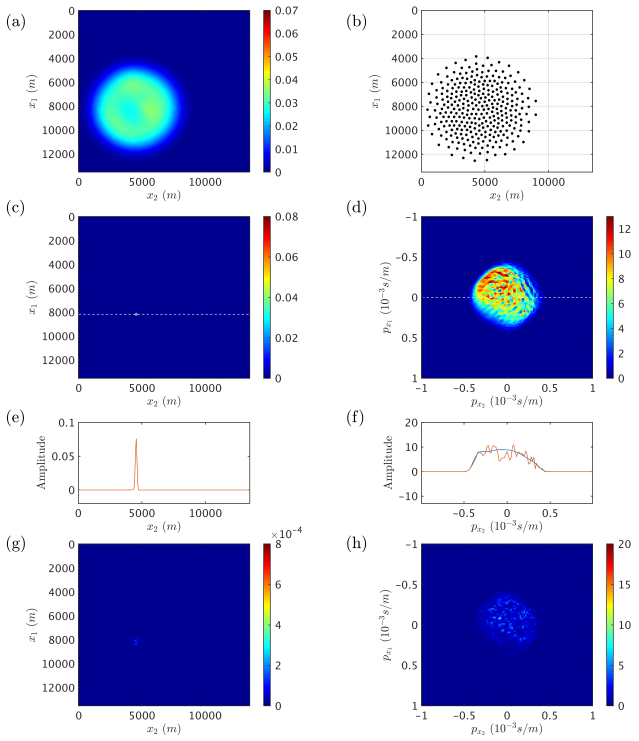

Fig. 14. Geometry optimization results using J_1 under the SEG/EAGE salt model: (a) optimized receiver density distribution, (b) optimized receiver geometry, (c) corresponding resolution function, and (d) AVP function. The dashed line in (c) and (d) indicates the cross section locations of plots (e) and (f). The red line in (e) and (f) represents the evaluated geometry, while the blue line represents the reference geometry. (g) and (h) Residuals of the resolution function and the AVP function, respectively, displayed in absolute scale.

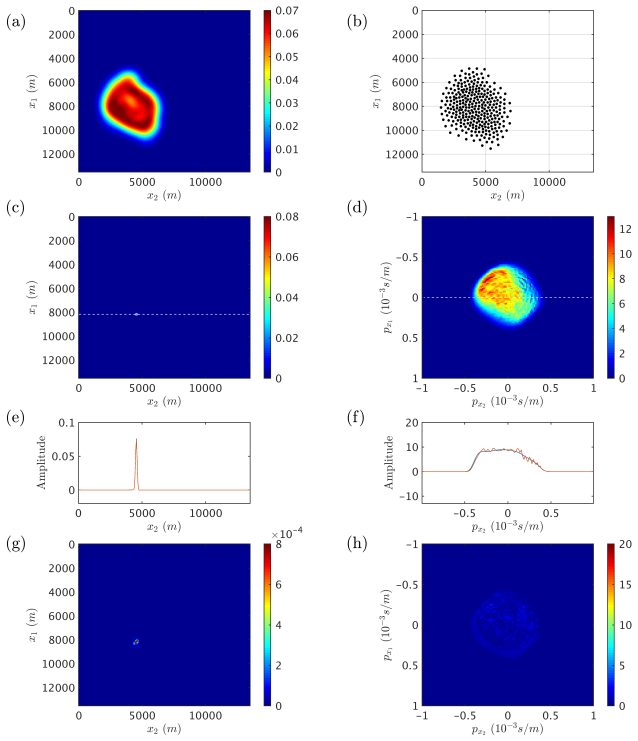

Fig. 15. Geometry optimization results using J_2 under the SEG/EAGE salt model: (a) optimized receiver density distribution, (b) optimized receiver geometry, (c) corresponding resolution function, and (d) AVP function. The dashed line in (c) and (d) indicates the cross section locations of plots (e) and (f). The red line in (e) and (f) represents the evaluated geometry, while the blue line represents the reference geometry. (g) and (h) Residuals of the resolution function and the AVP function, respectively, displayed in absolute scale.

the density optimized for J_2 achieves the highest amplitude accuracy over all azimuths and angles.

C. Velocity Error Analysis

Our acquisition design method requires the *a priori* knowledge of the subsurface, and the acquisition geometry is optimized for the input velocity model. A completely wrong velocity model could lead to an acquisition geometry that has an unacceptable illumination quality. In practice, a macrovelocity model is typically obtained from vintage seismic data, especially in a monitoring scenario. To analyze the influence of the velocity error, we use a velocity model that has been smoothed with a 600-m box of the velocity displayed in Fig. 11 as the input velocity model and optimize for J_2. Therefore, the reference focal functions and the update directions are computed using the smoothed velocity model instead of the true velocity model during optimization.

As a result, Fig. 17(a) and (b) shows the optimized density and geometry using J_2 with the smoothed velocity; Fig. 17(c)–(h) shows the focal functions that are computed using the true velocity model such that we can evaluate the true illumination quality. The optimized density has an irregular shape and is different from the optimized density using the true velocity in Fig. 15(a); the resolution function has a sharp peak in Fig. 17(c) and (e); and the misfit in Fig. 17(g) is small with the maximum being 0.8% of the scale of the resolution

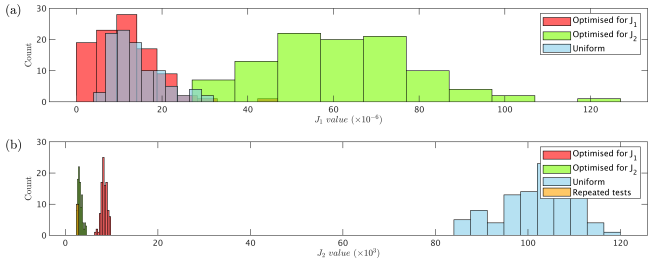

Fig. 16. (a) Histograms of J_1 values of 100 realizations of the receiver density optimized for J_1 (red), the density optimized for J_2 (green), and the uniform density (blue). (b) Histograms of J_2 values of 100 realizations of the density optimized for J_1 (red), the density optimized for J_2 (green), the uniform density (blue), and the one-bin histogram of the ten repeated tests of optimizing for J_2 (orange).

function. Compared to the optimization result in Fig. 15, the AVP function in Fig. 17(d) has detailed difference compared to Fig. 15(d); the residual in Fig. 17(h) has slightly higher error at approximately $(p_{x_1} = -0.3, p_{x_2} = 0.1) * 10^{-3}$ s/m compared to Fig. 15(h); and overall, the residual levels in Figs. 17(h) and 15(h) show similar quality of angle coverage. In addition, the histogram of 100 geometries transformed from the resulting density shows a similar J_2 distribution compared to the one obtained by using the true velocity model (see Fig. 18).

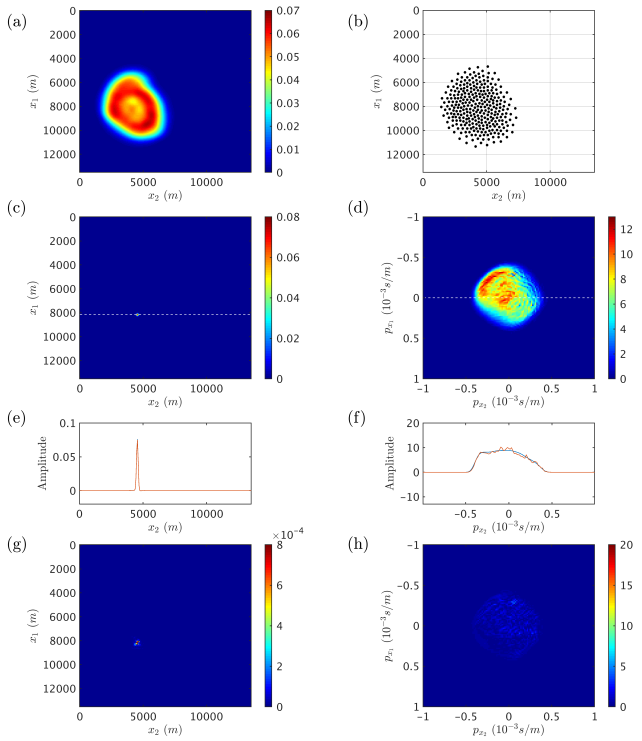

Fig. 17. Geometry optimization results using J_2 under the smoothed SEG/EAGE salt model: (a) optimized receiver density distribution, (b) optimized receiver geometry, (c) corresponding resolution function, and (d) AVP function that is computed with the true velocity model. The dashed line in (c) and (d) indicates the cross section locations of plots (e) and (f). The red line in (e) and (f) represents the evaluated geometry, while the blue line represents the reference geometry. The reference focal functions are computed using the true velocity model for comparison. (g) and (h) Residuals of the resolution function and the AVP function, respectively, displayed in absolute scale.

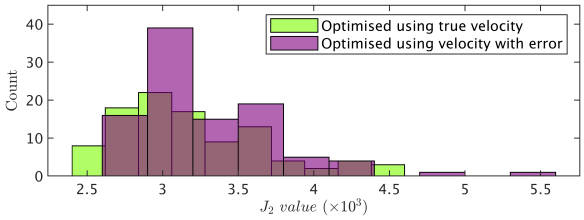

Fig. 18. Histograms of J_2 values of 100 realizations of the density optimized for J_2, using the true velocity (green) and the smoothed velocity model (purple).

V. Discussion

We have demonstrated that the proposed gradient method with several initial guesses is effective in designing a 3-D geometry for optimum illumination. In the examples of the SEG/EAGE salt model, we used four initial guesses, and the number of iterations for each individual process is typically 50; thus, the total number of iterations is 200. In comparison, a genetic algorithm needs 4500 evaluations of the objective function to reach a geometry solution of similar quality.

The reference AVP functions in Figs. 6(d) and 12(d) do not have flat spectra because we have a laterally varying velocity model, and we use the complex conjugate of the propagation operator as the migration operator in the calculation of focal functions. Hence, there is an imprint of the complex velocity in the AVP function. It is possible to include an illumination compensation or to use a least-squares migration in the focal function calculation to ensure a flat AVP spectrum. However, such applications are not expected to change much the optimization results because both the reference and the updated focal functions are calculated using the same migration operator.

The proposed gradient method does not guarantee a global minimum solution due to the nonlinear parameter-data relationship. In solving an acquisition design problem, we do not aim to obtain the global minimum. A local minimum is acceptable for an acquisition design problem since it provides improved illumination. With regard to the nonuniqueness of the geometry solutions, we expect additional constraints to reduce the ambiguity in solutions. In practice, we can generate a group of solutions that have a similar error and then choose one according to the acquisition preferences. For instance, the receivers can only be deployed in a certain area due to obstacles in the field; the inline direction of the marine streamer usually depends on the ocean flow direction. These extra constraints can help eliminate candidate geometries and reach realistic proposals.

Acquisition geometry design consists of designing both the source and the receiver geometries. In this article, we only discuss optimizing one side, being either sources or receivers. As demonstrated in the examples, we design the receiver geometry with the source side fixed. Likewise, the source geometry can be optimized with the receiver side fixed. The gradient expression for optimizing the source geometry would be (12) and (14) with $S(\mathbf{r}_s)$ being replaced by $D(\mathbf{r}_r)$. The method described in this article can be extended to optimizing both the source and receiver geometries simultaneously, where the source geometry is optimized for several iterations, then the receiver geometry is optimized with the latest source geometry for several iterations, and so on [32]. This procedure is similar to the double-loop inversion process described in [33].

One potential extension of the current method is to design for long-offset data only. Full-waveform inversion (FWI), widely commonly used technology in seismic velocity estimation, typically requires high-angle diving waves. An acquisition geometry that has a good angle coverage at high angles is likely to be beneficial for FWI. Shen *et al.* [34] have shown that the wide offsets of the OBN data were one of the key ingredients for the quality uplift in the FWI velocity model. For the geometry optimization, it is possible to apply a weight to favor the large angles in the AVP function and only invert for this weighted AVP function.

In this article, we have shown examples with a simplified scenario with no noise presence, a single target point, and a fixed receiver number. Noise is an important aspect to address in seismic acquisition design. In a land acquisition environment, the seismic data processing suffers tremendously from unsatisfactory signal-to-noise ratio, which is caused by strong surface-wave noise; and in a marine acquisition environment, the seismic data processing suffers more from surface multiple reflections. The quantitative models of how noise affects the

data quality should be established; after that, we can use them as the acquisition design criteria or include them in the existing design methods. Note that illumination is the only criterion used here. In practice, we also need to consider the impact of other processing techniques before imaging.

We have described the procedure of geometry optimization for only one target point due to the chosen forward model. In a seismic monitoring scenario, we typically focus on the reservoir volume, and hence, a grid of multiple target points can be chosen. The method described here can be extended to optimize the illumination for multiple target points by adding the objective function of each target point. The example of multiple target points is not included in this study due to high computational effort. In the examples shown in this article, the optimized sampling density tends to be nonuniform. When multiple target points are considered, the optimized sampling density is expected to become more averaged, depending on the extent of the subsurface target area. If the target area is relatively small and the overburden is complex, we expect a nonuniform density distribution. However, if the subsurface target area is large to the extent that the criterion becomes an overall good image of the entire subsurface, a different forward model should be chosen instead of the focal beam analysis for computational efficiency. For instance, a 3-D ray-trace modeling, such as the one described in [35], would be more suitable to assess the image quality of a large area in the subsurface. If the scope of acquisition is to obtain adequate velocity models of the subsurface, other approaches, such as [36], should be referred to.

A fixed number of receivers are chosen to reduce the nonlinearity of the optimization problem. With the current gradient method, the easiest way to incorporate an indefinite receiver number is to repeat the procedures in Fig. 3 or Algorithm 1 for several different receiver numbers. We can then compare the quality and the cost from different numbers of receivers. It is also possible to make the receiver number vary within a certain range, by adding a constraint on the total number of receivers to J_1 and J_2 in (11) and (13), respectively. However, keep in mind that a varying number of sampling points will make the optimization problem more nonlinear. A linearized algorithm is likely to end up in local minima. Further research is required for a global optimization algorithm incorporating such a constraint.

This methodology and the parameterization provide interesting opportunities in designing the location of ocean-bottom seismometers for crustal imaging purposes [37] or finding an optimum distribution of an earthquake monitoring network [38]. It requires the knowledge of the geological overburden, the location of the hypocenter, and the earthquake mechanism. The criterion would be redefined to suit the requirement in crustal imaging or earthquake monitoring. For instance, the forward model should include converted waves for crustal imaging. The gradient calculation would be modified according to the forward formulation; nevertheless, the inversion framework can stay the same. The sampling density, as a macrosolution of the geometry, provides the opportunity of a linearized framework, which is computationally efficient.

VI. Conclusion

We have proposed and demonstrated a methodology that can automatically optimize an irregular acquisition geometry for an improved target illumination under a complex overburden. The results indicate interesting geometry design strategies for two different requirements. When the requirement is resolution, the uniform geometry already has an acceptable resolution. When the requirement is angle coverage, an optimized geometry achieves a high amplitude accuracy over all azimuths and angles compared to the uniform geometry. In the optimization scheme, the parameter—sampling density—is a macrosolution of the acquisition geometry, which can be used for flexible acquisition systems, regular acquisition systems, and potentially automated devices. This parameterization allows us to use a linearized optimization algorithm via a gradient descent scheme to solve the acquisition design problem. The focal beam analysis provides the link between the subsurface and the target illumination for calculating the update. The proposed method is effective and computationally efficient.

Acknowledgment

The authors would like to thank the sponsors of the Delphi Consortium, Delft University of Technology (TU Delft), for the stimulating discussions at the consortium meetings. SEG and EAGE are thanked for providing the SEG/EAGE salt model. Adriaan Secord is acknowledged for the open-source software related to the weighted Voronoi diagram.

References

[1] G. J. Vermeer, *3D Seismic Survey Design*. Tulsa, OK, USA: Society of Exploration Geophysicists, 2002.

[2] M. Howard, "Marine seismic surveys with enhanced azimuth coverage: Lessons in survey design and acquisition," *Lead. Edge*, vol. 26, no. 4, pp. 480–493, 2007.

[3] W. Wei, L.-Y. Fu, J. Su, G. Liu, and W. Sun, "Numerical method for horizontal and vertical spatial resolutions of seismic acquisition geometries in complex 3D media," *IEEE Access*, vol. 8, pp. 116544–116555, 2020.

[4] D. Muerdter and D. Ratcliff, "Understanding subsalt illumination through ray-trace modeling, Part 3: Salt ridges and furrows, and the impact of acquisition orientation," *Lead. Edge*, vol. 20, no. 8, pp. 803–816, Aug. 2001.

[5] A. W. F. Volker, G. Blacquière, A. J. Berkhout, and L. Ongkiehong, "Comprehensive assessment of seismic acquisition geometries by focal beams—Part II: Practical aspects and examples," *Geophysics*, vol. 66, no. 3, pp. 918–931, May 2001.

[6] E. J. van Veldhuizen, G. Blacquière, and A. J. Berkhout, "Acquisition geometry analysis in complex 3D media," *Geophysics*, vol. 73, no. 5, pp. Q43–Q58, Sep. 2008.

[7] C. J. Regone, "Using 3D finite-difference modeling to design wide-azimuth surveys for improved subsalt imaging," *Geophysics*, vol. 72, no. 5, pp. SM231–SM239, Sep. 2007.

[8] J. Gardner, C. Lapilli, C. Xu, and A. González, "Finite difference wave-equation illumination: A deep-water case study," in *Proc. 82th Annu. Int. Meeting, Expanded Abstr.*, 2012, pp. 1–4.

[9] A. Kumar, G. Blacquière, M. W. Pedersen, and A. Goertz, "Full-wavefield marine survey design using all multiples," *Geophysics*, vol. 81, no. 3, pp. P1–P12, May 2016.

[10] A. Curtis, "Optimal design of focused experiments and surveys," *Geophys. J. Int.*, vol. 139, no. 1, pp. 205–215, Oct. 1999.

[11] J. van den Berg, A. Curtis, and J. Trampert, "Optimal nonlinear Bayesian experimental design: An application to amplitude versus offset experiments," *Geophys. J. Int.*, vol. 155, no. 2, pp. 411–421, Nov. 2003.

[12] D. A. Coles and F. D. Morgan, "A method of fast, sequential experimental design for linearized geophysical inverse problems," *Geophys. J. Int.*, vol. 178, no. 1, pp. 145–158, Jul. 2009.

[13] H. Maurer, A. Curtis, and D. E. Boerner, "Recent advances in optimized geophysical survey design," *Geophysics*, vol. 75, no. 5, pp. 75A177–75A194, 2010.
[14] T. Guest and A. Curtis, "On standard and optimal designs of industrial-scale 2-D seismic surveys," *Geophys. J. Int.*, vol. 186, no. 2, pp. 825–836, Aug. 2011.
[15] N. Vinard, N. K. Martiartu, C. Boehm, I. J. Balic, and A. Fichtner, "Optimized transducer configuration for ultrasound waveform tomography in breast cancer detection," in *Proc. SPIE Med. Imag. Ultrason. Imag. Tomogr.*, vol. 10580, Mar. 2018, Art. no. 105800I.
[16] M. Araya-Polo, M. Verschuren, and D. Hohl, "Target-oriented automatic shot selection," in *Proc. 86th Annu. Int. Meeting, SEG, Expanded Abstr.*, 2016, pp. 3855–3859.
[17] A. H. A. Latiff, D. P. Ghosh, and N. M. A. Latiff, "Optimizing acquisition geometry in shallow gas cloud using particle swarm optimization approach," *Int. J. Comput. Intell. Syst.*, vol. 10, no. 1, pp. 1198–1210, 2017.
[18] J. Su, L.-Y. Fu, W. Wei, J. Hu, and W. Sun, "Focal beam analysis for 3D acquisition geometries in complex media with GPU implementation," *Comput. Geosci.*, vol. 118, pp. 39–51, Sep. 2018.
[19] E. Bathellier and L. Haumonté, "The midwater stationary cable (FreeCable), a totally flexible acquisition technology to tackle the subsurface imaging and reservoir characterization challenges," in *Proc. 88th Annu. Int. Meeting, SEG, Expanded Abstr.*, pp. 66–70, 2018.
[20] A. J. Berkhout, L. Ongkiehong, A. W. F. Volker, and G. Blacquière, "Comprehensive assessment of seismic acquisition geometries by focal beams—Part I: Theoretical considerations," *Geophysics*, vol. 66, no. 3, pp. 911–917, May 2001.
[21] J. F. Claerbout, *Imaging the Earth's Interior*, vol. 1. Oxford, U.K.: Blackwell, 1985.
[22] D. Gisolf and E. Verschuur, *The Principles of Quantitative Acoustical Imaging*. Houten, The Netherlands: Eage, 2016.
[23] A. W. F. Volker, "Assessment of 3-D seismic acquisition geometries by focal beam analysis," Ph.D. dissertation, Dept. Imag. Phys., Delft Univ. Technol., Delft, The Netherlands, 2002.
[24] A. J. Berkhout, *Seismic Migration, Imaging of Acoustic Energy by Wave Field Extrapolation, A: Theoretical Aspects*. Amsterdam, The Netherlands: Elsevier, 1982.
[25] C. G. M. de Bruin, C. P. A. Wapenaar, and A. J. Berkhout, "Angle-dependent reflectivity by means of prestack migration," *Geophysics*, vol. 55, no. 9, pp. 1223–1234, Sep. 1990.
[26] A. Secord, "Weighted Voronoi stippling," in *Proc. 2nd Int. Symp. Non-Photorealistic Animation Rendering*, 2002, pp. 37–43.
[27] A. Okabe, B. Boots, K. Sugihara, and S. N. Chiu, *Spatial Tessellations: Concepts Application Voronoi Diagrams*, vol. 501. Hoboken, NJ, USA: Wiley, 2009.
[28] L. Knopoff and A. F. Gangi, "Seismic reciprocity," *Geophysics*, vol. 24, no. 4, pp. 681–691, 1959.
[29] H. Nyquist, "Certain topics in telegraph transmission theory," *Trans. Amer. Inst. Elect. Eng.*, vol. 47, no. 2, pp. 617–644, Apr. 1928.
[30] A. Fichtner, H. P. Bunge, and H. Igel, "The adjoint method in seismology: I. Theory," *Phys. Earth Planet. Interiors*, vol. 157, nos. 1–2, pp. 86–104, 2006.
[31] F. Aminzadeh, B. Jean, and T. Kunz, *3-D Salt and Overthrust Models*. Tulsa, OK, USA: Society of Exploration Geophysicists, 1997.
[32] S. Wu, E. Verschuur, and G. Blaquière, "Automated target-oriented acquisition design: Optimizing both source and receiver geometries," in *Proc. 89th Annu. Int. Meeting, SEG, Expanded Abstr.*, 2019, pp. 142–146.
[33] X. R. Staal, "Combined imaging and velocity estimation by joint migration inversion," Ph.D. dissertation, Dept. Imag. Phys., Delft Univ. Technol., Delft, The Netherlands, 2015.
[34] X. Shen, I. Ahmed, A. Brenders, J. Dellinger, J. Etgen, and S. Michell, "Full-waveform inversion: The next leap forward in subsalt imaging," *The Lead. Edge*, vol. 37, no. 1, pp. 67b1–67b6, 2018.
[35] A. A. Ibrahim, "3D ray-trace modeling to assess the effects of overburden and acquisition geometry on illumination of pre-evaporite reservoirs in karachaganak field, Kazakhstan," *Lead. Edge*, vol. 24, no. 9, pp. 940–944, Sep. 2005.
[36] V. Krampe, P. Edme, and H. Maurer, "Optimized experimental design for seismic full waveform inversion: A computationally efficient method including a flexible implementation of acquisition costs," *Geophys. Prospecting*, vol. 69, no. 1, pp. 152–166, Jan. 2021.
[37] C. Peirce and A. J. Day, "Ocean-bottom seismograph tomographic experiments—A consideration of acquisition geometries vs. resources," *Geophys. J. Int.*, vol. 151, no. 2, pp. 543–565, Nov. 2002.
[38] N. Rabinowitz and D. M. Steinberg, "Optimal configuration of a seismographic network: A statistical approach," *Bull. Seismol. Soc. Amer.*, vol. 80, no. 1, pp. 187–196, Feb. 1990.

Sixue Wu received the B.Sc. degree in geophysics from the China University of Geosciences, Wuhan, China, in 2012, the joint M.Sc. degree in applied geophysics from the Delft University of Technology, Delft, The Netherlands, ETH Zürich, Zürich, Switzerland, and RWTH Aachen University, Aachen, Germany, in 2014, and the Ph.D. degree from the Delft University of Technology in 2020.

As a member of the Delphi Consortium, Delft University of Technology, she is involved in the research topics of optimizing seismic acquisition. She is currently a Research Geophysicist with BP p.l.c., Sunbury-on-Thames, U.K.

Dirk J. (Eric) Verschuur received the M.Sc. and Ph.D. (Hons.) degrees in applied physics from the Delft University of Technology (DUT), Delft, The Netherlands, in 1986 and 1991, respectively.

From 1992 to 1997, he worked under a senior research fellowship from the Royal Dutch Academy of Art and Sciences (KNAW), Amsterdam, The Netherlands. In 1997, he became an Assistant Professor at the Department of Imaging Physics, DUT, where he has been an Associate Professor since 1999. He is currently the Director of the Delphi Research Consortium, DUT, which carries out research in the field of geoimaging, supported by 25 companies in the energy sector. His main interests are seismic modeling, data processing, and imaging techniques.

Dr. Verschuur received the Society of Exploration Geophysicists's (SEG's) J. Clarence Karcher Award in 1997. He was awarded the Virgil Kauffman Gold Medal from SEG in 2006.

Gerrit Blacquière received the M.Sc. and Ph.D. degrees in applied physics from the Delft University of Technology (DUT), Delft, The Netherlands, in 1985 and 1989, respectively.

From 1989 to 1993, he worked with the Delft Geophysical (currently part of WesternGeco), The Netherlands, where he developed depth migration algorithms. He was also involved in a research project focused on the "next-generation" seismic acquisition system. From 1993 to 2019, he worked at the Dutch research institute TNO, Den Haag, The Netherlands, where he had several management positions related to research and development. In 2006, he became an Associate Professor at the Earth Sciences Department (currently 60% appointment), DUT. He is currently the Project Leader of the Delphi Research Consortium on Acquisition and Preprocessing, DUT, where research is carried in the field of geoimaging for the energy sector in the area of seismic acquisition. His main interests are seismic modeling, acquisition, and (pre)processing techniques.